



THE UNIVERSITY *of* EDINBURGH

## Edinburgh Research Explorer

# Synchrotron X-ray nanotomographic and spectromicroscopic study of the tricalcium aluminate hydration in the presence of gypsum

### Citation for published version:

Geng, G, Myers, RJ, Yu, Y-S, Shapiro, DA, Winarski, RP, Levitz, P, Kilcoyne, ALD & Monteiro, PJM 2018, 'Synchrotron X-ray nanotomographic and spectromicroscopic study of the tricalcium aluminate hydration in the presence of gypsum', *Cement and Concrete Research*, vol. 111, pp. 130-137.  
<https://doi.org/10.1016/j.cemconres.2018.06.002>

### Digital Object Identifier (DOI):

[10.1016/j.cemconres.2018.06.002](https://doi.org/10.1016/j.cemconres.2018.06.002)

### Link:

[Link to publication record in Edinburgh Research Explorer](#)

### Document Version:

Peer reviewed version

### Published In:

Cement and Concrete Research

### General rights

Copyright for the publications made accessible via the Edinburgh Research Explorer is retained by the author(s) and / or other copyright owners and it is a condition of accessing these publications that users recognise and abide by the legal requirements associated with these rights.

### Take down policy

The University of Edinburgh has made every reasonable effort to ensure that Edinburgh Research Explorer content complies with UK legislation. If you believe that the public display of this file breaches copyright please contact [openaccess@ed.ac.uk](mailto:openaccess@ed.ac.uk) providing details, and we will remove access to the work immediately and investigate your claim.



**Synchrotron X-ray Nanotomographic and Spectromicroscopic Study of the  
Tricalcium Aluminate Hydration in the Presence of Gypsum**

Guoqing Geng<sup>1,2,\*</sup>, Rupert J. Myers<sup>1,3</sup>, Young-Sang Yu<sup>4</sup>, David A. Shapiro<sup>4</sup>, Robert  
Winarski<sup>5</sup>, Pierre E. Levitz<sup>6</sup>, David A.L. Kilcoyne<sup>4</sup>, Paulo J. M. Monteiro<sup>1,7</sup>

<sup>1</sup> Department of Civil and Environmental Engineering, University of California at  
Berkeley, Berkeley, California 94706, United States.

<sup>2</sup> Laboratory of Waste Management, Paul Scherrer Insitut, 5232 Villigen PSI,  
Switzerland

<sup>3</sup> University of Edinburgh, School of Engineering, King's Buildings, Sanderson Building,  
Edinburgh, EH9 3FB, United Kingdom.

<sup>4</sup> Advanced Light Source Lawrence Berkeley National Laboratory, Berkeley, California  
94720, United States.

<sup>5</sup> Center for Nanoscale Materials, Argonne National Laboratory, Argonne, Illinois 60439,  
United States.

<sup>6</sup> PHENIX lab, Sorbonne Université, UPMC Univ Paris 06, CNRS, Paris, France.

<sup>7</sup> Material Science Division-Lawrence Berkeley National Laboratory, Berkeley,  
California 94720, United States.

\* Correspondence and requests for materials should be addressed to Guoqing Geng  
(guoqing.geng@psi.ch).

## Abstract

The rheology of modern Portland cement (PC) concrete critically depends on the correct dosage of gypsum (calcium sulfate hydrate) to control the hydration of the most reactive phase - tricalcium aluminate ( $C_3A$ ). The underlying physio-chemical mechanism, however, remains unsolved mainly due to the lack of high-spatial-resolved and chemistry-sensitive characterization of the  $C_3A$  dissolution frontier. Here, we fill this gap by integrating synchrotron-radiation based crystallographic, photon-energy-dependent spectroscopic and high-resolution morphological studies of the  $C_3A$  hydration product layer. We propose that ettringite ( $6CaO \cdot Al_2O_3 \cdot SO_3 \cdot 32H_2O$ ) is the only hydration product after the initial reaction period and before complete gypsum dissolution. We quantify the 2D and 3D morphology of the ettringite network, e.g. the packing density of ettringite at various surface locations and the surface dissolution heterogeneity. Our results show no trace of a rate-controlling diffusion barrier. We expect our work to have significant impact on modeling the kinetics and morphological evolution of PC hydration.

## Key words

Tricalcium Aluminate, Hydration Products, Characterization, X-Ray Diffraction, Spectromicroscopy.

## 1. Introduction

Portland cement (PC) concrete is ubiquitous. The centrality of this technology to modern society is attributed to the low cost and global availability of the raw materials used in PC manufacture (mainly limestone and clay) and concrete production (water and aggregate,

e.g., sand and stone), its robustness, controllability and high performance [1]. Precisely controlled rheology of fresh PC concrete is fundamentally important to produce high quality and durable PC concrete infrastructure, which is essential to reduce its environmental impact [1-4]. Gypsum ( $\text{CaSO}_4 \cdot 2\text{H}_2\text{O}$ ) addition is critical to control the fluidity and overall time window of flowability of fresh PC concrete mixtures to avoid ‘flash setting’ [1,4-6] by retarding the hydration of the most reactive PC clinker phase – tricalcium aluminate ( $\text{C}_3\text{A}$ ).

The hydration of  $\text{C}_3\text{A}$  can be delayed by minutes to hours depending on the  $\text{C}_3\text{A}$  to calcium sulfate ratio in cement [1,2,5]. The resulting period of low reactivity enables a fresh concrete mixture to be flowable; however, the chemistry underlying this mechanism has not been completely elucidated despite being researched for over half a century [5,7-19]. This uncertainty has mostly persisted because direct evidence of this mechanism has not been reported. Two main hypotheses exist, which describe the inhibition of  $\text{C}_3\text{A}$  hydration to occur via: (i) the formation of an ettringite<sup>7</sup> ( $6\text{CaO} \cdot \text{Al}_2\text{O}_3 \cdot \text{SO}_3 \cdot 32\text{H}_2\text{O}$ )- and/or a Ca-Al layered double hydroxide (AFm, ‘alumino-ferrite-mono’)-type ‘diffusion barrier’ that physically blocks the  $\text{C}_3\text{A}$  surface from contacting the aqueous phase. The AFm phases are reported as monosulfate ( $4\text{CaO} \cdot \text{Al}_2\text{O}_3 \cdot \text{SO}_3 \cdot 18\text{H}_2\text{O}$ , also denoted as s-AFm) [8] and/or hydroxyl AFm (OH-AFm, mainly  $4\text{CaO} \cdot \text{Al}_2\text{O}_3 \cdot 19\text{H}_2\text{O}$  ( $\text{C}_4\text{AH}_{19}$ ) [9,10], which dehydrates to  $4\text{CaO} \cdot \text{Al}_2\text{O}_3 \cdot 13\text{H}_2\text{O}$  ( $\text{C}_4\text{AH}_{13}$ ) at a relative humidity  $< \sim 88\%$  [11,12], and gradually converts to  $3\text{CaO} \cdot \text{Al}_2\text{O}_3 \cdot 6\text{H}_2\text{O}$  ( $\text{C}_3\text{AH}_6$ ) over time [9]); or (ii) the adsorption of Ca and/or S complexes onto  $\text{C}_3\text{A}$  surface sites [13-15]. The latter hypothesis has recently gained increasing support although the ‘diffusion barrier’ hypothesis has not yet been disproven, due mainly to ettringite precipitates hindering a direct observation of the  $\text{C}_3\text{A}$  dissolution

frontier [16,17]. Therefore, a nanometer-resolved chemical-crystallographic probe is needed to more fully investigate the C<sub>3</sub>A dissolution frontier. Conventional imaging methods, including scanning electron microscopy (SEM) [18] and transmission electron microscopy (TEM) [19], are restricted by destructive sample preparation and electron beam damage. Three dimensional (3D) sub-micron scale characterization of the C<sub>3</sub>A dissolution frontier has also never been reported [20].

Recent advances in synchrotron-based experimental technology have substantially improved the ability to obtain direct chemical and morphological information in hydrated C<sub>3</sub>A systems: state-of-the-art soft X-ray ptychography imaging [21,22] coupled with scanning transmission X-ray microscopy (STXM), and X-ray adsorption near-edge fine structure (XANES) [23] now enables transmission imaging at ~5 nm pixel resolution and chemical (energy) mapping at ~70 nm pixel resolution [24,25], respectively. Here, we exploit this technology to reveal the mechanism by which C<sub>3</sub>A hydration is retarded in the presence of gypsum (with a C<sub>3</sub>A-to-gypsum mass ratio = 1 : 0.4, and a water-to-solid mass ratio = 10), aiming to identify features with sizes on the order of tens of nm at the C<sub>3</sub>A dissolution frontier. These data are complemented by three-dimensional (3D) tomograms reconstructed from full-field transmission X-ray microscopy (TXM) data at a voxel resolution ~20 nm<sup>3</sup> [26]. Crystallographic information is also obtained using in-situ wide angle X-ray scattering (WAXS). Small angle scattering (SAS) data is calculated from the X-ray ptychographic images [27,28] and compared with in-situ small angle X-ray scattering (SAXS) results, to obtain quantitative morphological information of the reacting C<sub>3</sub>A particle surface boundaries. The implications of these results on the contemporary

understanding of the dissolution-retarding effect of gypsum on C<sub>3</sub>A hydration, and on the computer-based cement hydration modeling are then discussed.

## **2. Experimental**

### **2.1 Materials**

Pure C<sub>3</sub>A and hydrogarnet (C<sub>3</sub>AH<sub>6</sub>) powders were purchased from Mineral Research Processing (<http://www.mineralresearchprocessing.fr/>). Gypsum was purchased from Fisher Scientific (#S76764). The purities of these materials were verified by powder X-ray diffraction (XRD) (see SI for details). The C<sub>3</sub>A powder has a size distribution from 1 µm to 100 µm, with  $d_{50} \sim 20$  µm [15]. Partially-hydrated C<sub>3</sub>A samples were prepared by mixing gypsum, C<sub>3</sub>A and ‘nanopure’ water ( $1.82 \times 10^7$  Ω cm, produced using a Barnstead NANOpure II with a filter size = 0.2 µm) in sealed plastic vials at room temperature ( $25 \pm 2$  °C). The samples were agitated frequently by hand and/or constantly by mechanical rotation. An initial mass ratio of C<sub>3</sub>A to gypsum of 1 : 0.4 was used. A w/s = 10 was selected to fit the requirement of most experiments, and a w/s = 1 was also used for the X-ray ptychography experiments to verify the influence of sample dilution. Ettringite and s-AFm were independently prepared by precipitation from stoichiometric mixtures of C<sub>3</sub>A, gypsum and water, following the reported methods [29]. The identities of these reference minerals were confirmed by XRD, as shown in the Supplementary Information (SI).

### **2.2 SEM**

C<sub>3</sub>A powder was spread on carbon tape pieces attached to steel SEM sample holders, which were then submerged into saturated gypsum-water solution. After certain hydration time (80s and 160s), the hydrated samples were then immediately rinsed with large quantities

of 99.5% ethanol and dried in N<sub>2</sub> atmosphere to prevent carbonation. Samples were carbon coated before observation, using a Zeiss EVO™ in second electron mode at 5 keV and 7 pA.

### **2.3 STXM and Al *K*-edge XANES**

The STXM experiments were conducted at beamline 5.3.2.1 of the ALS (Advanced Light Source) of LBNL (Lawrence Berkeley National Laboratory) [21], which operates at 1.9 GeV and 500 mA using a bending magnet source and an active servo-stabilized toroidal pre-mirror that generates 10<sup>7</sup> photons per second at the sample location. The resolving power of the radiation source is  $E/\Delta E \sim 5000$ . Following the sample preparation method in previous work [30], partially hydrated C<sub>3</sub>A samples prepared as described above were drop-cast onto 100 nm-thick Si<sub>3</sub>N<sub>4</sub> windows (Norcada™), with excess solution removed using Kimwipes (Kimtech Science™). Samples were immediately transferred to the vacuumed STXM chamber. Single absorption contrast images were collected at an incident beam energy of 1575 eV (close to the Al *K*-edge). Stacks of absorption contrast images were recorded from 1552 to 1605 eV with step size 0.1 eV from 1565 to 1594 eV and step size 0.3 eV over the bordering central energy ranges of this investigation. A dwell time of 3 s was used. The image stack was aligned and analyzed with the aXis2000 software [31]. As reference minerals, hydrogarnet was dispersed with acetone whereas ettringite and s-AFm were dispersed with nanopure water, drop-cast and measured similarly. Internal calibration was conducted by calibrating the background absorption maximum to 1560 eV.

### **2.4 X-ray ptychography**

X-ray ptychography imaging was conducted using the same STXM setup used for the Al *K*-edge XANES experiments. For these measurements, a 60 nm outer zone width zone plate

focused a coherent soft X-ray beam (750 eV) onto the sample, which was scanned in 40 nm increments to ensure overlap of the probed areas. The effects of incoherent background signals were eliminated by implementing a background retrieval algorithm that iteratively determines a constant offset to the diffraction data. The sample was aligned with respect to the zone plate through an interferometric feedback system. A pixel size of 5 nm was used in image reconstruction. The efficient image resolution is determined to be ~17 nm by Fourier Ring Correlation (FRC; see SI for details) [32]. Small angle scattering calculations were performed using the ptychography images as input (the algorithm is available in SI).

## **2.5 In-situ WAXS and SAXS**

In-situ WAXS and SAXS experiments were conducted at the WAXS/SAXS beamline of the Synchrotron Light Research Institute (SLRI), Thailand, which runs at 1.2 GeV and 75-125 mA. For the measurements, an incident beam of 9 keV was transmitted through two pieces of kapton™ film between which the sample was placed, encompassing samples from 2 to 120 minutes of hydration. The  $q$ -range covered was 0.04 to 42 nm<sup>-1</sup> for WAXS and 0.07 to 0.7 nm<sup>-1</sup> for SAXS, both with an angular step size of 0.25°.

## **2.6 TXM tomography**

The TXM projections were collected at the Hard X-ray Nanoprobe Beamline, operated by the Center for Nanoscale Materials at Sector 26 of the Advanced Photon Source [26]. A cluster of partially-hydrated C<sub>3</sub>A samples was mounted on a tungsten needle tip and placed on a multi-directional scanning stage. The incident beam was tuned to 9 keV and condensed by an elliptically shaped single-reflection glass capillary with a central stop. Transmission images were recorded while the sample was rotated from -90° to 90°. Ten images were collected at every 1° step, with an exposure of 10 s at each step to obtain better statistics.



All tomographic 3D volume reconstructions were performed by an algebraic reconstruction technique (ART) with 20 iterations [33]; see details in SI.

### 3. Results

#### 3.1 In-situ WAXS study of the initial hydration.

Fig. 1a-1c are the SEM images of the initial hydration of  $C_3A$  particles in calcium sulfate solution that is saturated with respect to gypsum. The surface morphology changes greatly over a few minutes. The first dominant hydration product has a foil/flake-like morphology, which coats the  $C_3A$  particles within the first minute ( $\leq 80$  s), but is then quickly masked by needle-like ettringite precipitates by 160 s (Fig. 1c). The initially formed flake-like precipitates are 200-300 nm thick at their edges (Fig. 1b) and are reported to be poorly-crystalline AFm phases [9,35]. The initial formed needles are short (Fig. 1b), but with similar diameter as the abundant ettringite that formed later on. Synchrotron-radiation based in-situ WAXS, with peaks assigned based on published results [36-41] detects only the diffraction of remnant  $C_3A$  and gypsum, and a small quantity of ettringite here, from 2 to 120 minutes of hydration (Fig. 1d). The intensities of the major  $C_3A$  and gypsum diffraction peaks vary slightly with respect to the absolute values, whereas the intensity of ettringite diffraction increases monotonically with increasing hydration time (Fig. 1d, inset). The characteristic peaks of OH-AFm (e.g.,  $C_4AH_{19}$ ) at 10.7 Å, ( $8.3^\circ$ , red arrow in Fig. 1d) [39], and s-AFm at 8.97 Å ( $9.9^\circ$ , blue arrow in Fig. 1d) [40], are not observed during the first 120 minutes of hydration, indicating that the initially-formed AFm-type flakes, if initially formed, remain poorly crystalline, or are gradually decomposed with increasing hydration time. They do not seem to convert to  $C_3AH_6$  (4.44, 3.35 and 3.14 Å (i.e.  $20.1^\circ$ ,  $26.6^\circ$  and  $28.4^\circ$ , respectively, green arrows in Fig. 1d) [41]). A previous

synchrotron radiation XRD study of a similar system also revealed no trace of crystallized AFm-type phases before gypsum is completely consumed [42]. However, AFm-type crystals form immediately after mixing solid and water at a much lower initial gypsum-to- $C_3A$  ratio [10]. It seems that the crystallinity of the AFm-type phase depends largely on the dynamics of ion concentration change at the beginning of hydration.

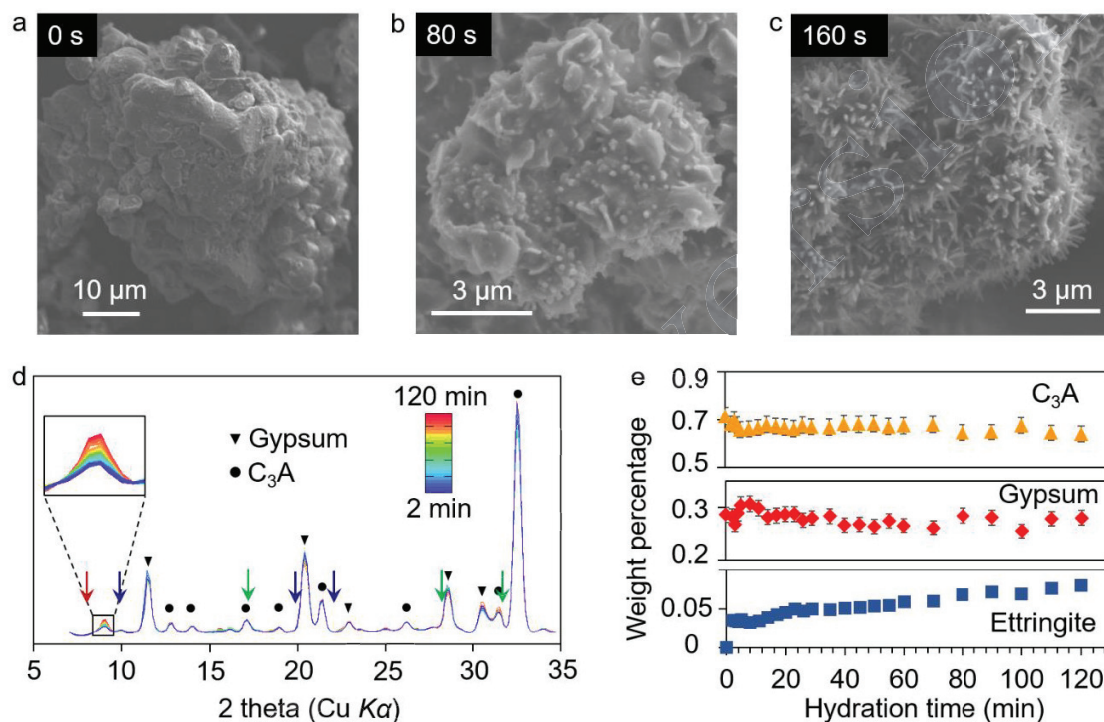


**Fig. 1.** SEM and in-situ WAXS characterization of  $C_3A$  hydration in the presence of gypsum. SEM images of  $C_3A$  particles before hydration (a), and hydrated for 80 s (b) and 160 s (c). (d) In-situ WAXS results of a sample ( $C_3A$  to gypsum mass ratio = 1 : 0.4) hydrated for 2 to 120 minutes, plotted in color series.  $C_3A$  and gypsum diffraction peaks are labelled with triangles and circles, respectively. The inset shows the evolution of the major diffraction peak of ettringite. The red, blue and green arrows denote the unobserved characteristic diffraction peaks of  $C_4AH_{19}$ , s-AFm and  $C_3AH_6$ , respectively. (e) Evolution of the mass percentages of ettringite, gypsum and  $C_3A$  during hydration determined using Rietveld refinement, estimated relative error =  $\pm 5\%$ .

Mass percentages of individual phases in the crystalline component of the reacted sample are calculated through Rietveld refinement (Fig. 1d); see details in SI. A quick

initial dissolution of  $C_3A$  is observed during the first 10 min. The dissolution of gypsum is slower with respect to  $C_3A$ , since the percentage of gypsum clearly rises within the first 10 min. There is an initially observed ettringite formation ( $\sim 3.5$  wt%) at 2 min, which remains nearly unchanged within the first 10 min. Considering the low Al concentration in the liquid [16], the dissolved Al from  $C_3A$  most likely precipitates as Al-bearing phases of low sulfur content, for instance  $AH_3$  and AFm. This is consistent with the observation of previous in-situ XRD study on cement hydration [43,44]. After the first 10 min, a slow and steady rate of ettringite formation as well as gypsum and  $C_3A$  dissolution is observed, until 120 min. Ettringite forms at a rate of  $\sim 2$  wt% per hour with respect to the total crystalline solid mass, reaching 8 wt% at 120 min. After 120 min hydration, the weight ratio of ettringite-to- $C_3A$  is 0.125 (Fig. 1e). The average diameter of  $C_3A$  particles is  $\sim 20$   $\mu m$  [15]. If the surface of  $C_3A$  particle is smooth, the volume of ettringite divided by  $C_3A$  surface area is  $\sim 2.8$   $\mu m^3/\mu m^2$ , using the existing density data [36-37]. As shown in Fig. 1b, the formation of flake-like precipitates in the first minute precedes the significant precipitation of ettringite needles. Therefore, it is unlikely that they act as a physical barrier to retard the precipitation of ettringite within the first 2 minutes of hydration. However, it is still unclear whether an AFm-type layer persists as a physical barrier surrounding  $C_3A$  particles throughout the low-reactivity period, as it may be XRD-transparent, or masked by ettringite needles in the SEM images.

### 3.2 XANES Spectromicroscopic study

To further identify the solid phases, regardless of their crystallinity, on partly hydrated  $C_3A$  surface, we collected the Al  $K$ -edge XANES spectra of eight regions parallel to the  $C_3A$

dissolution frontier (B1-B8 in Fig. 2a,) using nanometer resolved STXM. For comparison, XANES spectra of pure solid phases relevant to the  $C_3A$ -gypsum- $H_2O$  system were also measured and presented. In the Al  $K$ -edge XANES spectra, peaks A, C and E correspond to the transitions of  $1s$  to  $3s$ -like,  $3p$ -like and  $3d$ -like states, respectively, and peak D corresponds to multi-scattering within adjacent neighbor shells [45]. The transition of the  $1s$  to the  $3s$  state is forbidden by the selection rule but is observable if the tetrahedron coordination is distorted and permits a mixture of Al  $s$  and  $p$  states, which is observed here. In good agreement with other Al-bearing minerals [45-48], the position of peak C, as shown in Fig. 2b, is a few eV lower for tetrahedral Al (Al[4]), i.e., in  $C_3A$  [36], than for octahedral Al (Al[6]), i.e., in solid hydration products such as ettringite [37], s-AFm [40],  $C_4AH_{13}$  [11] (dehydration of  $C_4AH_{19}$  is likely to occur in vacuum conditions [12]) and  $C_3AH_6$  [41]. The unique features of the reference spectra allow us to determine the identity of the solid hydration products.

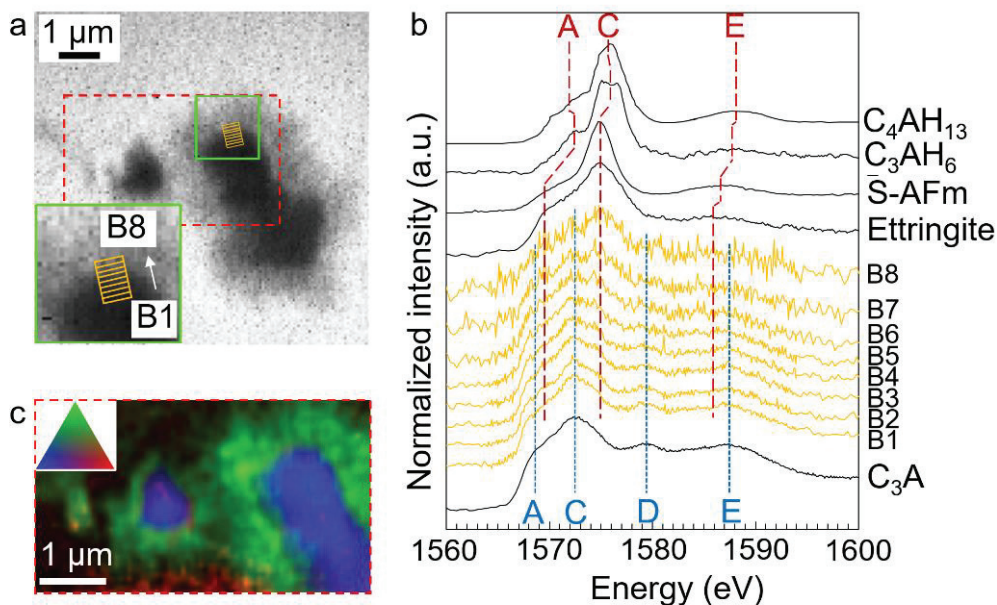


**Fig. 2** STXM and Al K-edge XANES results for C<sub>3</sub>A hydrated for 150 minutes in the presence of gypsum. (a) An X-ray absorption contrast image at 1575 eV, with XANES data collected for each pixel (the pixel size is  $\sim 70 \times 70$  nm). Eight segments ( $\sim 100 \times 700$  nm each), marked by yellow rectangles labelled B1 (bottom) to B8 (top) (inset in a), are selected to sample a continuous region at the C<sub>3</sub>A dissolution frontier that includes unreacted C<sub>3</sub>A and solid hydration products (the inset is a magnification of the green-boxed region in the main image). (b) Al K-edge of XANES spectra for each area of B1-B8 (yellow curves), and the reference spectra for C<sub>3</sub>A and several possible Al-containing solid hydration products [2,4]. Resonance peaks for Al[4] and Al[6] are marked by short-dashed blue and long-dashed red lines, respectively. The spectrum of C<sub>4</sub>AH<sub>13</sub> is adapted from published work [47]. (c), Phase composition mapping of the region outlined by the dashed red rectangle in (a), where green, blue and red shaded areas correspond to ettringite, C<sub>3</sub>A and decomposition residue, respectively. Inset is a RGB color-triangle for reader convenience.

In the Al K-edge XANES spectra of B1-B8, the intensities of the Al[4] peaks (blue short dashed lines) A (1568.6 eV), C (1572.5 eV), D (1579.3 eV) and E (1587.4 eV) shrink and the Al[6] peaks (red long dashed lines) C (1574.9 eV) and E (1585.9 eV) grow as functions of increasing distance away from the C<sub>3</sub>A particle (Fig. 2b). The spectra collected in regions B1 and B2 are almost identical to the Al K-edge XANES spectrum of C<sub>3</sub>A, which show strong intensities at the energies of its major tetrahedral Al (Al[4]) peaks A, C, D and E, indicating that these regions contain predominantly remnant C<sub>3</sub>A. The positions of the growing Al[6] peaks C and E in B1-B8 match with the corresponding peaks and positions for ettringite (1574.9 and 1585.9 eV respectively) rather than C<sub>3</sub>AH<sub>6</sub> (1576.0 and 1588.0 eV respectively) or C<sub>4</sub>AH<sub>13</sub> (1575.8 and 1588.2 eV respectively). Compared to the intensities and shapes of peaks C and A in the spectrum for ettringite, peak C (1574.7 eV) is significantly sharper and peak a (1569.4 eV) is much weaker in the spectrum of s-AFm. Therefore, regions B3–B6 contain significant amounts of C<sub>3</sub>A (Al[4]) and ettringite (Al[6]) and regions B7–B8 contain predominantly ettringite (Al[6]). After 150 minutes of hydration, ettringite is the only precipitate observed in the dissolution frontier of the C<sub>3</sub>A particle analyzed here.

The Al *K*-edge XANES of the full imaged region is well-fitted using the spectra of C<sub>3</sub>A (blue) and ettringite (green), with only a small residual signal (red) in the background region that is thus assigned to measurement noise (Fig. 2c). This result further demonstrates that ettringite is the only solid hydration product here at 150 minutes of hydration. There is no trace of AFm phases, although flake-like AFm dominate the surface morphology at initial hydration (Fig. 1b). There is also no trace of C<sub>3</sub>AH<sub>6</sub> that is expected to precipitate from the destabilization of OH-AFm phases. This ettringite layer is ~1 μm thick on the bigger C<sub>3</sub>A particle (Fig. 2a, right), and slightly thinner on the smaller one (Fig. 2a, left).

### **3.3 Quantifying nano-morphology using X-ray ptychographic imaging and in-situ SAXS**

X-ray ptychographic imaging is used to observe the morphology of the C<sub>3</sub>A dissolution frontier (Fig. 3). The image resolution is determined to be ~17 nm by Fourier ring correlation; see SI. Needle-like ettringite precipitates studied here are observed with similar thickness from 30 to 620 minutes of hydration in the water to solid mass ratio (w/s) = 10 system (Fig. 3a-3c). The population of ettringite needles increases with increasing hydration time, but individual needles generally all grow to a maximum length of ~1 μm and do not seem to thicken significantly. Ettringite prefers to nucleate on C<sub>3</sub>A particles, and generally grow perpendicular to the C<sub>3</sub>A surface (dashed blue squares). The needle network is increasingly densified through interlacing of ettringite needles in confined regions (dashed yellow squares). By 620 minutes of hydration, the layer of ettringite needles are observed to directly contact the remnant C<sub>3</sub>A surface, i.e., no continuous physical barrier is observed in the interfacial zone (inset in Fig. 3c).



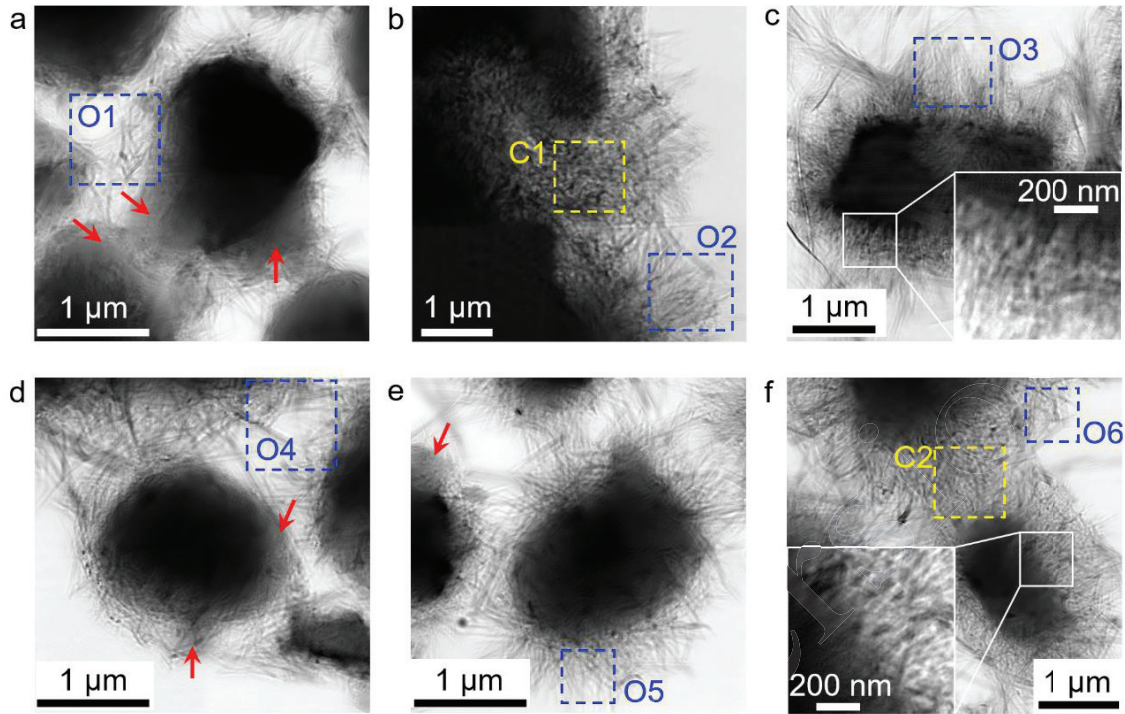


**Fig. 3** X-ray ptychographic images of  $C_3A$  hydrated in the presence of gypsum and  $w/s = 10$  (a-c), and  $w/s = 1$  (d-f), at hydration times of: (a) 30 min; (b) 135 min; (c) 620 min; (d) 30 min; (e) 90 min; and (f) 910 min. The pixel size is  $5 \times 5 \text{ nm}^2$ . Blue and yellow squares indicate needle-like ettringite precipitation on open  $C_3A$  surfaces and confined spaces between particles, respectively. Red arrows indicate a gel-like hydration product that is observed at early hydration only. The insets in c and f are magnified regions of the interface between remnant  $C_3A$  and hydration product (white boxes).

The morphologies of the  $C_3A$  dissolution frontier in the  $w/s = 10$  (Fig. 3a-3c) and  $w/s = 1$  (Fig. 3d-3f) systems are similar. Ettringite needles reach a length of  $\sim 1 \mu\text{m}$  after 910 minutes of hydration and thicken negligibly in the  $w/s = 1$  system. A solid ‘diffusion barrier’ is not identified at 910 minutes of hydration (Fig. 3f inset).  $C_3A$  hydration kinetics is reported to be independent of the  $w/s$  between 1 and 10 [16,49]. In both  $w/s$  systems, there exist continuous ‘gel-like’ areas (red arrows in Fig. 3a, 3d and 3e) on the particle surfaces that have distinct grey scale values compared to the remnant  $C_3A$  and with dimension of a few hundred nanometers. They are observed to be abundant at a relatively

early age of hydration, and intermixed with ettringite needles on the  $C_3A$  surface. These gel-like morphologies are highly consistent with the flake-like AFm gel as shown in SEM images (Fig. 1b). However, this gel is not observed at a later age of hydration under the transmission microscope (Fig. 3b, 3c and 3f), indicating that the initially formed AFm flakes are unstable, and may dissolve to feed the precipitation of ettringite during the low-reactivity period. Therefore, the initially formed AFm gel is unable to act as the physical barrier described in the ‘diffusion barrier’ hypothesis to retard  $C_3A$  dissolution throughout the low-reactivity period as stated in the introduction. This interpretation is consistent with the STXM and Al  $K$ -edge XANES results.

To quantify the morphology of the ettringite needles that precipitate under different degrees of spatial confinement, theoretical calculations of SAS (algorithm available in SI) are applied to the selected dashed blue (O1-O6, less confined) and yellow (C1-C2, more confined) square regions in Fig. 3, and are compared with in-situ SAXS measurements of the  $w/s = 1$  system (Fig. 4). The calculated SAS results generally resemble the in-situ SAXS results, and both can be interpreted using the form factor of a typical Guinier-Porod pattern of agglomerated isometric rods or cylinders [50]. This provides strong evidence that the needle-like morphology of ettringite at the  $C_3A$  dissolution frontier is not an artefact of drying, which is suggested to alter the surface morphology of hydrated PC particles [51]. In a log-log plot of the intensity vs. scattering vector ( $q$ ), the  $q_1$  and  $q_{cutoff}$  values define the lower and higher end, respectively, of a linear Porod region with slope between -4 and -3, corresponding to the surface fractal dimension. For  $q < q_1$ , a nonlinear Guinier region with slope ranging from -1 to -3 is inferred, which corresponds to the volume fractal dimension. Due to the limitation of the SAXS experimental setup and the overall size of the selected



ptychographic image regions ( $\sim 1 \mu\text{m}^2$  here), the low- $q$  end of the Guinier region here is not small enough to reliably probe the length scale equal to or larger than the needle length (i.e.,  $> 1 \mu\text{m}$ ).

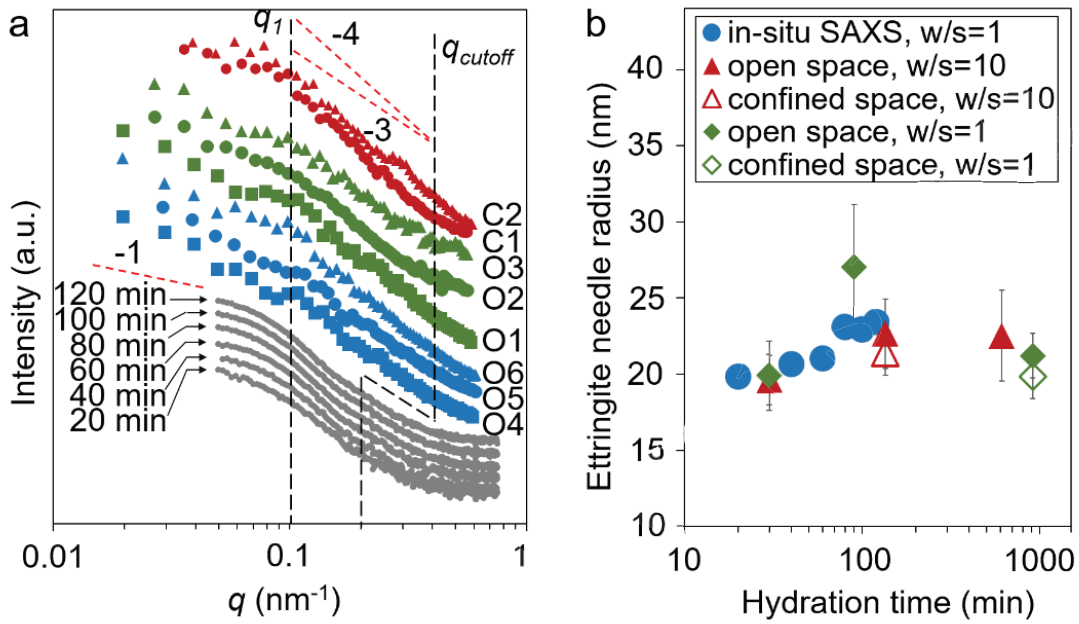


**Fig. 4** Quantifying the morphology of  $\text{C}_3\text{A}$  particles hydrated in the presence of gypsum using SAS. (a) In-situ SAXS results from 20 to 120 minutes of hydration, using the SAXS at a hydration time of 2 minutes as the background signal, which is comprised mainly of liquid water,  $\text{C}_3\text{A}$  and gypsum. SAS were also calculated from the regions marked by dashed squares in the ptychographic images (Fig. 3). The  $q_1$  (intersection between lower- $q$  Guinier region and higher- $q$  Porod region) and  $q_{\text{cutoff}}$  (high- $q$  end of Porod region) are schematically marked with black long-dashed lines. Red short-dashed lines with slope -4 and -3 are displayed as eye guides only. (b) Evolution of the radii of the needle-like ettringite precipitates, with the uncertainty denoted by error bars and marker size. The uncertainty is derived from the fitting of  $q_1$  and  $d$ .

As shown in Fig. 1c and Fig. 3, the needle-like ettringite precipitates are similarly sized.

In an isometric rod model, the radius ( $r$ ) of the rod can be related to  $q_1$  following eq.(1) [50]:

$$q_1 = (2d-2)^{0.5}/r \quad (1)$$

where  $d$  is the fractal dimension of the Porod region (further details regarding the interpretation of the SAXS data are presented in the SI), i.e., the absolute value of the slope when the logarithm of the intensity (base 10) is plotted as a function of  $q$  (Fig. 4a). The fitted needle radius,  $r$ , from the in-situ SAXS measurement increases slightly as a function of hydration time, i.e., from ~20 nm at 20 minutes of hydration to ~23 nm at 120 minutes of hydration, with a standard error of ~0.7 nm (Fig. 4b). A comparable result was obtained from the SAS data calculated from the ptychographic images at both  $w/s = 1$  and 10, where the radii of ettringite crystallites was determined to be  $\sim 23 \pm 5$  nm (Fig. 4b). Needles in confined space (C1-C2) are of similar thickness to those growing in open space (O1-O6). Therefore, before complete dissolution of gypsum (i.e.,  $< \sim 10$  hours), the typical radius of ettringite precipitates is  $< 30$  nm, and is independent of the  $w/s$  and hydration time; similarly the aspect ratio of ettringite needles is generally around 40. As hydration progresses, the growth of ettringite crystals is mainly through new precipitates on the  $C_3A$  surface, rather than the thickening or lengthening of individual ettringite needles.

### 3.4 Quantifying 3D morphology using nano-CT

To date, only 2D nano- and meso-scale morphologies of hydrated  $C_3A$  have been reported, providing limited morphological information on the  $C_3A$  dissolution frontier. To further probe the 3D nano-scale morphology of the  $C_3A$  dissolution frontier, a full-field TXM tomographic study was conducted to yield a 3D image at a voxel resolution of 20 nm, as shown in Fig. 5, where the blue and green colors represent  $C_3A$  and ettringite, respectively. A movie of the volume rendering is presented in the SI. The segmentation of the

background, ettringite and remnant  $C_3A$  was based on the reconstructed optical density  
 $(OD_{recon})$  histogram of the 3D image. Further details of the procedures are in the SI.

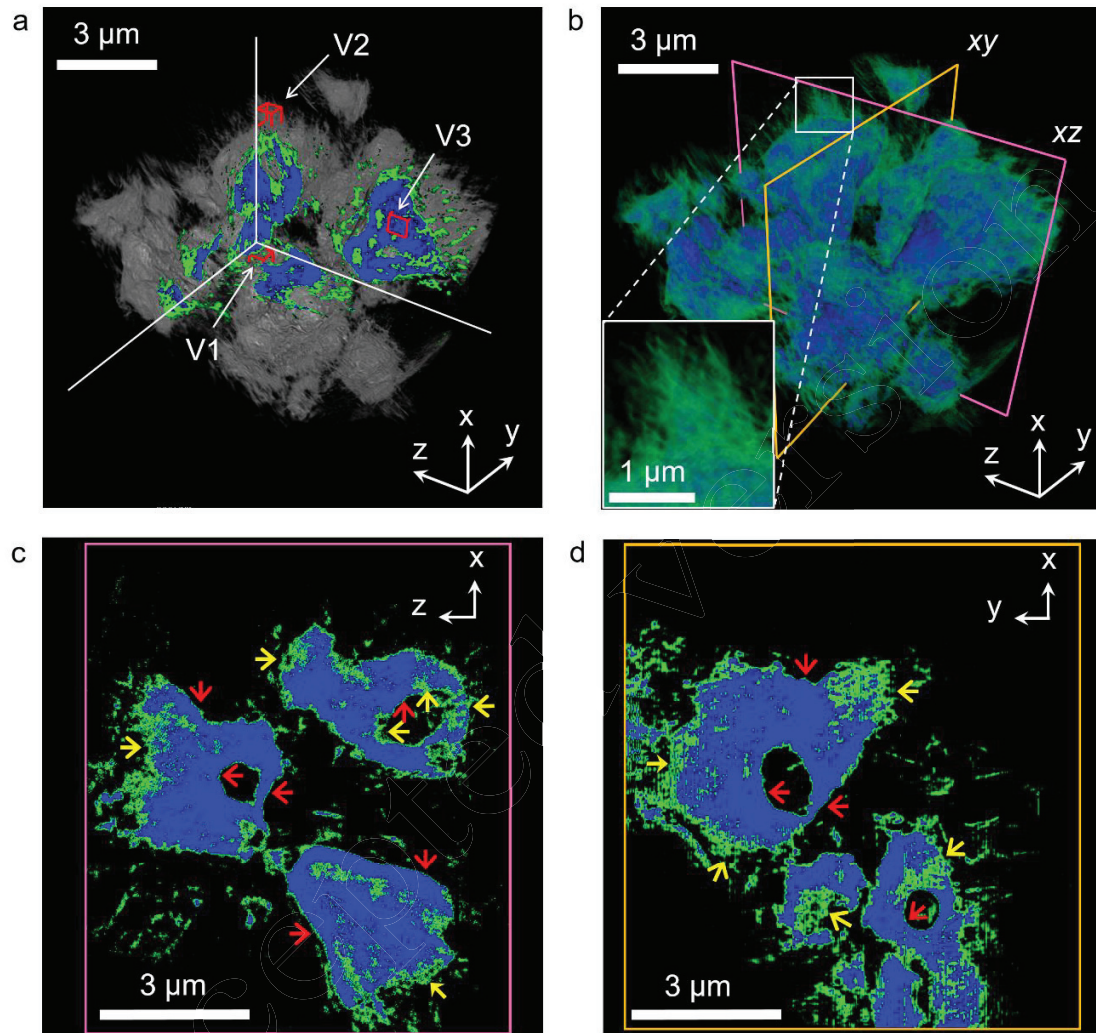


**Fig. 5** 3D reconstruction of  $C_3A$  particles hydrated for 143 minutes in the presence of gypsum. (a) A cubic sub-volume (white lines represent its edges) is removed from the full 3D dataset to expose interior features, which are colored blue (remnant  $C_3A$ ) and green (solid hydration products). The reconstructed voxel volume is  $20 \times 20 \times 20 \text{ nm}^3$ . Sub-volumes V1, V2 and V3 (unfilled red cubes of 600 nm edge length) correspond to hydration products grown in confined space, open space, and remnant  $C_3A$ , respectively. (b) Colored volume rendering of remnant  $C_3A$  (blue) and hydration product (green). A magnified region is shown in the white box inset. Two slices, marked by pink and orange squares, are displayed in (c) (xz plane) and (d) (xy plane), respectively. Segmentation of hydration products and remnant  $C_3A$  is performed by applying a threshold optical density value according to the histogram of the full 3D data (further details are available in the SI).

387

388 As calculated from the segmented 3D image, the volume of the ettringite and remnant  
389  $C_3A$  are  $\sim 40 \mu m^3$  and  $\sim 52 \mu m^3$ , respectively. By simplifying the  $C_3A$  particles in Fig. 5 as  
390 4 agglomerated particles with roughly spherical shape and smooth surface, the total surface  
391 area of  $C_3A$  is  $\sim 27 \mu m^2$ . The volume of ettringite to the calculated surface area of remnant  
392  $C_3A$  is thus  $\sim 1.5 \mu m^3/\mu m^2$ . This value is in the same order of magnitude as estimated using  
393 quantitative analysis of WAXS data, i.e.  $\sim 2.8 \mu m^3/\mu m^2$ , and therefore suggests that the  
394 segmentation is reasonable. However, by directly counting the surface area using the  
395 segmented 3D image of  $C_3A$ , its surface area is  $\sim 249 \mu m^2$ , which is one magnitude larger  
396 than the estimated value by assuming a smooth  $C_3A$  surface. This discrepancy indicates  
397 that the partially dissolved  $C_3A$  surface is very rough.

398 The result shows that  $C_3A$  particles are non-uniformly reacted at 143 minutes of  
399 hydration (Fig. 5), with the solid hydration products on  $C_3A$  surfaces varying in thickness  
400 up to 1-1.5  $\mu m$ , with some surface areas barely covered. This information is not observed  
401 in the 2D X-ray ptychographic images (Fig. 3) as they are transmission images.  
402 Heterogeneous  $C_3A$  dissolution is observed to generate sub-micron scale features,  
403 including highly reacted and rough surface regions (yellow arrows in Fig. 5c and 5d) and  
404 much smoother surfaces with low reaction extents (red arrows in Fig. 5c and 5d). There  
405 seems to be no intermediate status, i.e., the  $C_3A$  surface either dissolves extensively to form  
406 needle-like precipitations of constant maximum length ( $\sim 1.5 \mu m$ ), or stays almost  
407 unreacted. From a visual estimation, the highly dissolved  $C_3A$  surface area is about 40%  
408 of its total surface area at a hydration age of 143 min. In some low-reaction surface regions,  
409 the green color layer is of single voxel thickness, which is not necessarily a thin layer of

ettringite. In fact, the transmission images with higher resolution shown no evidence of such continuous layers (Fig. 3c and 3f). Therefore they are most-likely due to artifacts of the segmentation due to the voxels on the  $C_3A$  surface containing both solid and void regions.

Surfaces of inner cavities are also reactive. Any originally closed cavities participate in hydration as soon as the dissolution frontier exposes them to the solution. Non-uniform hydration is also observed in the inner cavities of remnant  $C_3A$  particles (Fig. 5c and 5d), some of which are more connected to the external particle surface than others. The amount of reactive  $C_3A$  surface is directly related to the speed of ettringite formation [16]. Here, the TXM results show that the significant proportion of  $C_3A$  surface reacts at very slow rate which highlights the non-uniform nature of  $C_3A$  surface dissolution and hydration, observed on both external surface and internal cavity surface.

Porosities of selected sub-volumes in Fig. 5a, V1 (solid hydration products grown in confined space), V2 (solid hydration products grown in open space) and V3 (remnant  $C_3A$ ), are determined according to the attenuation law [52]. In the SI, we show that the porosity,  $\varphi$ , can be estimated using eq.(2):

$$\varphi = 1 - OD_{recon\_mean} / OD_{recon\_max} \quad (2)$$

where  $OD_{recon\_mean}$  is the average reconstructed optical density of the studied sub-volumes, and  $OD_{recon\_max}$  is the reconstructed optical density of a zero-porosity voxel of the studied phase (ettringite or  $C_3A$ ); see further details in the SI. By applying this equation to the three sub-volumes, we determine the respective porosities of V1, V2 and V3 to be 53-67%, 73-81% and 20%-38%. Therefore, after 143 minutes of hydration, the network of ettringite needles in open  $C_3A$  spaces (V2) is highly porous, and the network of ettringite needles in

confined spaces (V1) is denser but also significantly porous. The region representing remnant C<sub>3</sub>A (V3) contains non-zero porosity that may be caused by the presence of initial cavities.

The porosity of the cementitious binder critically influences its physical properties, and is therefore a key target of hydration modelling [1,2]. In a randomly packed rod network, the volume fraction of solid rods decreases with their increasing aspect ratio, reaching ~10% when the aspect ratio is ~40 [53]. Here, the volume fractions of ettringite needles on C<sub>3</sub>A surface estimated using the 3D image is ~2-5 times the value in the randomly packed case, indicating that the ettringite needles are systematically oriented. Previous studies of ettringite-water suspension indicate that the ettringite volume fraction  $\phi$  and the rod aspect ratio are related to various rheological properties such as suspension viscosity and the onset rate of shear thinning [54]. Therefore, this characterization of porosity and hydration product geometry on the sub-30 nm length scale, the first of its kind, can be used to develop and validate detailed 3D computational models of C<sub>3</sub>A hydration, nano-structure and rheology, a substantial step-change to a higher level of detail compared to existing formulations.

## 5. Discussion

Our results provide strong evidence that OH-AFm and s-AFm do not greatly retard the initial formation of ettringite as ettringite forms rapidly after a few minutes of hydration when most of the C<sub>3</sub>A surface is already covered by amorphous AFm phases. These AFm phases also do not form a C<sub>3</sub>A dissolution-inhibiting ‘diffusion-barrier’ in the low-reactivity period, because ettringite is identified by coupled STXM and Al K-edge XANES



as the only precipitate on C<sub>3</sub>A particles after 150 minutes of hydration, but before complete gypsum dissolution. The initially formed AFm phases destabilize completely to ettringite during the low-reactivity period. At an imaging resolution of ~15 nm, no obvious 'diffusion-barrier' is observed at the C<sub>3</sub>A dissolution frontier after the initial hydration period. Our X-ray ptychography and TXM results also show that the ettringite needle network at the C<sub>3</sub>A dissolution frontier is highly porous. The porosities of this network are 53-67% and 73-81% in confined and open spaces after 143 min of hydration, respectively, meaning that it does not act as a physical barrier to retard C<sub>3</sub>A hydration, in contradiction to the 'diffusion barrier' hypothesis. Therefore, the results point toward an alternative mechanism of C<sub>3</sub>A dissolution retardation, e.g., by adsorption of Ca and/or S complexes onto C<sub>3</sub>A surface sites [8,15,55].

The morphology of the C<sub>3</sub>A dissolution frontier in the presence of gypsum in aqueous solution is similar in systems with w/s = 1 and 10. In both cases, ettringite precipitation predominantly occurs via the production of more individual surface-bound needles rather than the existing needles increasing in thickness and length. Ettringite needles with radii of ~20 nm are observed after 20 min of hydration and grow to ~25 nm thick by 15 hours hydration; and the length of individual ettringite needles remain ~1  $\mu$ m. The independence of the needle size on the w/s suggests that it is not the free space which determines the size of needle. The growth of ettringite needles may be determined by the solution chemistry facts close to nucleation sites, instead of the bulk liquid region far away from C<sub>3</sub>A surface. A maximum growth length is also observed for the hydration products of tricalcium silicate (C<sub>3</sub>S), calcium silicate hydrates, which is suggested to be merely determined by the solution chemistry [56].

On the other hand, the 3D image clearly indicates that the  $C_3A$  surface either undergoes substantial dissolution to form needles of 1-1.5  $\mu m$  length, or otherwise stays essentially unreacted. This heterogeneity indicates that  $C_3A$  dissolution is also somewhat controlled by its crystalline surface chemistry and morphology [55]. Similar observation was reported recently for the hydration of a polished  $C_3A$  surface [57]. The dissolution of mineral surfaces are often promoted by the surface concentration of defects, such as roughness, grain boundaries and dislocations [58]. As indicated by Fig. 5, the dominating surface defect seems to be heterogeneously distributed at the micron-scale, and varies from facets to facets of the  $C_3A$  particles. This could be either the difference of roughness (amount of kinks) created during the grinding process, or the different cleavages (with different dissolution rate) created during the sintering process. However, we are unable to identify individual surface defects due to the limit of resolution.

Upon the above discussion, we now have a general picture of the studied reaction. When  $C_3A$  surface is in contact with sulfur-containing water solution, it undergoes quick dissolution and formation of an AFm-type gel, followed by the long low-reactivity period. In the low-reactivity period, the AFm-type gel quickly vanishes, and  $C_3A$  surface dissolution is very slow probably due to ion-complexation. Along with the slow dissolution, as soon as a defect site is exposed to solution, there is a localized quick dissolution of  $C_3A$ , followed by the quick growth of ettringite until a certain size. In the surface regions where less defects exist, ettringite formation is hardly observed. In future work, two processes need urgent investigation in order to quantitatively predict the  $C_3A$  hydration: 1) the dissolution of a single defect site on  $C_3A$  surface, 2) the mechanism that ettringite only grows to a certain size.



For the first time, this paper provides a sub-30 nm 2D and 3D morphological and spectroscopic study of the C<sub>3</sub>A dissolution frontier in the presence of gypsum during the low-reactivity period. It advances the understanding of cubic C<sub>3</sub>A hydration in the presence of gypsum, through the central quantification of the chemistry and morphology of hydration product on C<sub>3</sub>A surface. This work also serves as a preliminary step to studying PC hydration with sub-30 nm resolution synchrotron radiation technologies. We expect that these techniques will provide key experimental evidence to validate multi-scale computational simulations of PC hydration down to the nano-scale [59-61], and also the macro-scale properties of fresh PC concrete [54,62].

#### **Supporting information**

The supporting information available as a separate file, which includes the characterization of the raw materials, process of analyzing the WAXS and SAXS data, reconstruction and segmentation of the 3D TXM result, estimating the resolution of the ptychography images, and determining the peak positions of the XANES results. A video of the 3D rendering of the TXM result is also provided.

#### **Acknowledgments**

This work is funded by the Singapore-Berkeley Building Efficiency and Sustainability in the Tropics (SinBerBEST) Program. The authors acknowledge the support received from Ubonwan Khopongpaiboon, Panod Viseshchitra and Thanakrit Chandra (Siam Cement, Thailand), and from Siriwat Soontaranon (SAXS beamline of Synchrotron light research institute, Thailand). The Advanced Light Source was supported by the Director, Office of

Science, Office of Basic Energy Sciences, of the U.S. Department of Energy under Contract No. DE-AC02-05CH11231. Use of the Center for Nanoscale Materials and the Advanced Photon Source, both Office of Science user facilities, was supported by the U.S. Department of Energy, Office of Science, Office of Basic Energy Sciences, under Contract No. DE-AC02-06CH11357. The authors want to acknowledge Jeffrey W. Bullard (NIST, USA) for the insightful discussion on  $C_3A$  hydration. Guoqing Geng's PhD study is supported by the Chinese Scholarship Council (file No. 201206090127).

## References

1. P.K. Mehta, P.J.M. Monteiro, Concrete Microstructure, Properties, and Materials, McGraw-Hill Companies, New York City, ed. 4, 2014.
2. P. Barnes, J. Bensted, Structure and Performance of Cements, CRC Press, Boca Raton, ed. 2, 2002.
3. G.P. Peters, G. Marland, C. Le Quéré, T. Boden, J. G. Canadell, M. R. Raupach, Rapid growth in  $CO_2$  emissions after the 2008-2009 global financial crisis. Nature Clim. Change. 2 (2012) 2-4.
4. Mehta, P. K. Reducing the Environmental Impact of Concrete. Concr. Int. 23 (2001) 61-66.
5. H.F.W. Taylor, Cement Chemistry; Thomas Telford: London, 2<sup>nd</sup> edition, 1997.
6. E.B. Nelson, Well Cementing. Development of Petroleum Science, Vol. 28; Newnes: Boston, MA, 1990.
7. M. Collepardi, G. Baldini, M. Pauri, M. Corradi, Tricalcium aluminate hydration in the presence of lime, gypsum or sodium sulfate. Cem. Concr. Res. 8 (1978) 571-580.

- 553 8. J.W. Bullard, H.M. Jennings, R.A. Livingston, A. Nonat, G.W. Scherer, J.S.  
554 Schweitzer, K.L. Scrivener, J.J. Thomas, Mechanisms of cement hydration. Cem.  
555 Concr. Res. 41 (2011) 1208-1223.
- 556 9. L. Black, C. Breen, J. Yarwood, C.S. Deng, J. Phipps, G. Maitland, Hydration of  
557 tricalcium aluminate ( $C_3A$ ) in the presence and absence of gypsum — studied by  
558 Raman spectroscopy and X-ray diffraction. J. Mater. Chem. 16 (2006) 1263-1272.
- 559 10. A.N. Christensen, T.R. Jensen, N.V. Scarlett, I.C. Madsen, J.C. Hanson, Hydrolysis of  
560 pure and sodium substituted calcium aluminates and cement clinker components  
561 investigated by in situ synchrotron X-ray powder diffraction. J. Am. Ceram. Soc. 87  
562 (2004) 1488-1493.
- 563 11. E. Aruja, The unit cell and space group of  $4CaO \cdot Al_2O_3 \cdot 19H_2O$  polymorphs. Acta  
564 Cryst. 14 (1961) 1213-1216.
- 565 12. M.H. Roberts, New calcium hydrates. J. Appl. Chem. 7 (1957) 543-546.
- 566 13. M.E. Tadros, W.Y. Jackson, J. Skalny, Study of the dissolution and electrokinetic  
567 behavior of tricalcium aluminate. Colloid Interface Sci. 4 (1976) 211-223.
- 568 14. J. Skalny, M.E. Tadros, Retardation of tricalcium aluminate hydration by sulfates. J.  
569 Am. Ceram. Soc. 60 (1977) 174-175.
- 570 15. R.J. Myers, G. Geng, J. Li, E. D. Rodríguez, J. Ha, P. Kidkhunthod, G. Sposito, L.N.  
571 Lammers, A. P. Kirchheim, P. J. M. Monteiro, The role of adsorption phenomena in  
572 cubic tricalcium aluminate dissolution. Langmuir, 33 (2016) 45-55.
- 573 16. H. Minard, S. Garrault, L. Regnaud, A. Nonat, Mechanisms and parameters controlling  
574 the tricalcium aluminate reactivity in the presence of gypsum. Cem. Concr. Res. 37  
575 (2007) 1418-1426.

- 576 17. A. Quennoz, K.L. Scrivener, Hydration of  $C_3A$  – gypsum systems. *Cem. Concr.*  
577 *Res.* 42 (2012) 1032-1041.
- 578 18. R. Holly, H. Peemoeller, M. Zhang, E. Reardon, C. M. Hansson, Magnetic resonance  
579 in situ study of tricalcium aluminate hydration in the presence of gypsum. *J. Am.*  
580 *Ceram. Soc.* 89 (2006) 1022-1027.
- 581 19. C.J. Hampson, J.E. Bailey, The Microstructure of the hydration products of tri-calcium  
582 aluminate in the presence of gypsum. *J. Mater. Sci.* 18 (1983) 402-410.
- 583 20. M.D. Jackson, J. Moon, E. Gotti, R. Taylor, S.R. Chae, M. Kunz, A.H. Emwas, C.  
584 Meral, P. Guttman, P. Levitz, H.R. Wenk, Material and elastic properties of Al-  
585 tobermorite in ancient Roman seawater concrete. *J. Am. Ceram. Soc.* 96 (2013) 2598-  
586 2606.
- 587 21. D.A. Shapiro, Y.S. Yu, T. Tyliszczak, J. Cabana, R. Celestre, W. Chao, K.  
588 Kaznatcheev, A.L.D. Kilcoyne, F. Maia, S. Marchesini, Y.S. Meng, Chemical  
589 composition mapping with nanometre resolution by soft X-ray microscopy. *Nature*  
590 *Photon.* 8 (2014) 765-769.
- 591 22. Y.S. Yu, C. Kim, D.A. Shapiro, M. Farmand, D. Qian, T. Tyliszczak, A.D. Kilcoyne,  
592 R. Celestre, S. Marchesini, J. Joseph, P. Denes, Dependence on crystal size of the  
593 nanoscale chemical phase distribution and fracture in  $Li_xFePO_4$ . *Nano Lett.* 15 (2015)  
594 4282-4288.
- 595 23. A.L.D. Kilcoyne, T. Tyliszczak, W.F. Steele, S. Fakra, P. Hitchcock, K. Franck, E.  
596 Anderson, B. Harteneck, E.G. Rightor, G.E. Mitchell, A.P. Hitchcock, Interferometer-  
597 controlled scanning transmission X-ray microscopes at the Advanced Light Source. *J.*  
598 *Synchrotron Radiat.* 10 (2003) 125-136.

24. G. Geng, R. Taylor, S. Bae, D. Hernández-Cruz, A.L.D. Kilcoyne, A.H. Emwas, P.J.M. Monteiro, Atomic and nano-scale characterization of a 50-year-old hydrated C<sub>3</sub>S paste. *Cem. Concr. Res.* 77 (2015) 36-46.
25. G. Geng, J. Li, Y. S. Yu, D.A. Shapiro, A.L.D. Kilcoyne, P.J.M. Monteiro, Nanometer-resolved spectroscopic study reveals the conversion mechanism of CaO·Al<sub>2</sub>O<sub>3</sub>·10H<sub>2</sub>O to 2CaO·Al<sub>2</sub>O<sub>3</sub>·8H<sub>2</sub>O and 3CaO·Al<sub>2</sub>O<sub>3</sub>·6H<sub>2</sub>O at an elevated temperature. *Cryst. Growth Des.* 17 (2017) 4246-4253.
26. R.P. Winarski, M.V. Holt, V. Rose, P. Fuesz, D. Carbaugh, C. Benson, D. Shu, D. Kline, G.B. Stephenson, I. McNulty, J.A. Maser, Hard X-ray nanoprobe beamline for nanoscale microscopy. *J. Synchrotron Radiat.* 19 (2012) 1056-1060.
27. S. Brisard, R.S. Chae, I. Bihannic, L. Michot, P. Guttman, J. Thieme, G. Schneider, P.J.M. Monteiro, P. Levitz, Morphological quantification of hierarchical geomaterials by X-ray nano-CT bridges the gap from nano to micro length scales. *Am. Mineral.* 97 (2012) 480-483.
28. P. Levitz, D. Tchoubar, Disordered porous solids: from chord distributions to small angle scattering. *J. Phys. I.* 2, (1992) 771-790.
29. T. Matschei, B. Lothenbach, F.P. Glasser, The AFm Phase in Portland Cement, *Cem. Concr. Res.* 37 (2007) 118-130.
30. G. Geng, R. J. Myers, A.L. Kilcoyne, J. Ha, P.J.M. Monteiro, Ca L<sub>2,3</sub>-edge near edge X-ray absorption fine structure of tricalcium aluminate, gypsum and calcium (sulfo)aluminate hydrates. *Am. Mineral.* 102 (2017) 900-908.

31. A.P. Hitchcock, P. Hitchcock, C. Jacobsen, C. Zimba, B. Loo, E. Rotenberg, J. Denlinger, R. Kneedler, aXis 2000 — Analysis of X-ray images and spectra. <http://unicorn.mcmaster.ca/aXis2000.html>.
32. M. Van Heel, M. Schatz, Fourier shell correlation threshold criteria. *J. Struct. Biol.* 151 (2005) 250-262.
33. R. Gordon R. Bender, G.T. Herman, Algebraic reconstruction techniques (ART) for three-dimensional electron microscopy and X-ray photography. *J. Theor. Biol.* 29 (1970) 471-481.
34. A.C. Kak, M. Slaney, Principles of Computerized Tomographic Imaging, Society for Industrial and Applied Mathematics, Philadelphia, 2001.
35. P. Meredith, A.M. Donald, N. Meller, C. Hall, Tricalcium aluminate hydration: microstructural observations by in-situ electron microscopy. *J. Mater. Sci.* 39 (2004) 997-1005.
36. P. Mondal, J.W. Jeffery, The crystal structure of tricalcium aluminate,  $\text{Ca}_3\text{Al}_2\text{O}_6$ . *Acta Cryst. B* 31 (1975) 689-697.
37. A.E. Moore, H.F.W. Taylor, Crystal Structure of Ettringite. *Acta Cryst. B* 26 (1970) 386-393.
38. P. Comodi, S. Nazzareni, P.F. Zanazzi, S. Speziale, High-pressure behavior of gypsum: a single-crystal X-ray study. *Am. Mineral.* 93 (2008) 1530-1537.
39. T.R. Jensen, A.N. Christensen, J.C. Hanson, Hydrothermal transformation of the calcium aluminum oxide hydrates  $\text{CaAl}_2\text{O}_4 \cdot 10\text{H}_2\text{O}$  and  $\text{Ca}_2\text{Al}_2\text{O}_5 \cdot 8\text{H}_2\text{O}$  to  $\text{Ca}_3\text{Al}_2(\text{OH})_{12}$  investigated by in situ synchrotron X-ray powder diffraction. *Cem. Concr. Res.* 35 (2005) 2300-2309.

- 643 40. R. Allmann, Refinement of the hybrid layer structure  $[\text{Ca}_2\text{Al}(\text{OH})_6] \cdot [\frac{1}{2}\text{SO}_4 \cdot 3\text{H}_2\text{O}]^+$ .  
644 Neues. Jb. Miner. Monat. 3 (1977) 136-144.
- 645 41. G.A. Lager, T. Armbruster, J. Faber, Neutron and X-ray diffraction study of  
646 hydrogarnet  $\text{Ca}_3\text{Al}_2(\text{O}_4\text{H}_4)_3$ . Am. Mineral. 72 (1987) 756-765.
- 647 42. M. Merlini, G. Artioli, T. Cerulli, F. Cella, A. Bravo, Tricalcium aluminate hydration  
648 in additivated systems. A crystallographic study by SR-XRPD. Cem. Concr. Res. 38  
649 (2008) 477-486.
- 650 43. C. Hesse, F. Goetz-Neunhoeffler, J. Neubauer, A new approach in quantitative in-situ  
651 XRD of cement pastes: Correlation of heat flow curves with early hydration  
652 reactions. Cem. Concr. Res. 41 (2011) 123-128.
- 653 44. D. Jansen, F. Goetz-Neunhoeffler, C. Stabler, J. Neubauer. A remastered external  
654 standard method applied to the quantification of early OPC hydration. Cem. Concr.  
655 Res. 41 (2011) 602-608.
- 656 45. D. Li, G.M. Bancroft, M. Fleet, X. Feng, Y. Pan, Al K-edge XANES spectra of  
657 aluminosilicate minerals. Am. Mineral. 80 (1995) 432-440.
- 658 46. D.R. Neuville, G.S. Henderson, L. Cormier, D. Massiot, The structure of crystals,  
659 glasses, and melts along the  $\text{CaO-Al}_2\text{O}_3$  join: results from Raman, Al L- and K-edge  
660 X-ray absorption, and  $^{27}\text{Al}$  NMR spectroscopy. Am. Mineral. 95 (2010) 1580-1589.
- 661 47. M. Vespa, E. Wieland, R. Dähn, D. Grolimund, A.M. Scheidegger, Determination of  
662 the elemental distribution and chemical speciation in highly heterogeneous  
663 cementitious materials using synchrotron-based micro-spectroscopic  
664 techniques. Cem. Concr. Res. 37 (2007) 1473-1482.

- 665 48. N. Richard, N. Lequeux, P. Boch, EXAFS study of refractory cement phases:  
666  $\text{CaAl}_2\text{O}_4\text{H}_{20}$ ,  $\text{Ca}_2\text{Al}_2\text{O}_3\text{H}_{16}$ , and  $\text{Ca}_3\text{Al}_2\text{O}_{12}\text{H}_{12}$ . J. Phys. III 5 (1995) 1849-1864.
- 667 49. N. Tenoutasse, The hydration mechanism of  $\text{C}_3\text{A}$  and  $\text{C}_3\text{S}$  in the presence of calcium  
668 chloride and calcium sulfate. Proceedings of the 5<sup>th</sup> International Symposium on the  
669 Chemistry of Cement, 1968.
- 670 50. B. Hammouda, New Guinier-Porod Model. J. Appl. Cryst. 43 (2010) 716-719.
- 671 51. P.C. Fonseca, H.M. Jennings, The effect of drying on early-age Morphology of C-S-  
672 H as observed in environmental SEM. Cem. Concr. Res. 40 (2010) 1673-1680.
- 673 52. J.H. Hubbell, S.M. Seltzer, Tables of X-ray Mass Attenuation Coefficients 1 keV to  
674 20 MeV for Elements  $Z=1$  to 92 and 48 Additional Substances of Dosimetric Interest,  
675 National Institute of Standards and Technology, Interagency/Internal Report 5632,  
676 Gaithersburg, 1995.
- 677 53. A.P. Philipse, The random contact equation and its implications for (colloidal) rods in  
678 packings, suspensions, and anisotropic powders. Langmuir, 12 (1996) 1127-1133.
- 679 54. C.M. Vladu, C. Hall, G.C. Maitland, Flow properties of freshly prepared ettringite  
680 suspensions in water at 25° C. J Colloid Interface Sci. 294 (2006) 466-472.
- 681 55. W. Stumm, Reactivity at the mineral-water interface: dissolution and inhibition.  
682 Colloids Surf. A 120 (1997) 43-166.
- 683 56. K.L. Scrivener, P. Juilland, P.J.M. Monteiro, Advances in understanding hydration of  
684 portland cement. Cem. Concr. Res. 78 (2015) 38-56.
- 685 57. A.S. Brand, J.W. Bullard, Dissolution kinetics of cubic tricalcium aluminate measured  
686 by digital holographic microscopy. Langmuir. 8 (2017).



- 687 58. A. Lüttge, R.S. Arvidson, C.A. Fischer, Stochastic treatment of crystal dissolution  
688 kinetics. *Elements*. 9 (2013) 183-188.
- 689 59. D.P. Bentz, Three-dimensional computer simulation of portland cement hydration and  
690 microstructure development. *J. Am. Ceram. Soc.* 80 (1997) 3-21.
- 691 60. S. Bishnoi, K.L. Scrivener, *mic*: A new platform for modelling the hydration of  
692 cements. *Cem. Concr. Res.* 39 (2009) 266-274.
- 693 61. J.W. Bullard, E. Enjolras, W.L. George, S.G. Satterfield, J.E. Terrill, A parallel  
694 reaction-transport model applied to cement hydration and microstructure  
695 development. *Model. Simul. Mater. Sci. Eng.* 18 (2010) 025007.
- 696 62. F.J. Ulm, O. Coussy, Modeling of thermochemomechanical couplings of concrete at  
697 early ages. *J. Eng. Mech-ASCE*. 121 (1995) 785-794.